MDPI

Article

Effect of Oxygen in Mo-TM (TM = Ti, Zr, Hf) Solid Solutions as Studied with Density Functional Theory Calculations

Rachid Stefan Touzani, Rostyslav Nizinkovskyi [ID] and Manja Krüger *[ID]

Institute of Materials and Joining Technology, Otto-von-Guericke University Magdeburg, Universitätsplatz 2, 39106 Magdeburg, Germany; rachid.touzani@ovgu.de (R.S.T.); rostyslav.nizinkovskyi@ovgu.de (R.N.)
* Correspondence: manja.krueger@ovgu.de

Abstract: Mo-Ti-Si, Mo-Zr-B, and Mo-Hf-B are promising alloy systems for high-temperature applications as they show higher toughness and higher creep resistance than other Mo-based alloys. Regarding ductility and toughness, the chemical composition of the Mo solid-solution phase is the main parameter with which to tweak these properties of multiphase Mo-based alloys. Besides the common solid-solution hardening, one goal is to minimize embrittlement by decreasing the detrimental effects of interstitials like oxygen atoms in Mo alloys, which might be present in the bulk material due to trapping. For a better understanding of the trapping mechanisms and behavior of Mo solid solutions, the bonding situation and interaction of Mo atoms with the atoms of the alloying partners, as well as oxygen atoms, is worthwhile to investigate. For this, an in-depth analysis of the chemical bonding situation with calculations based on density functional theory in selected Mo-TM(-O) (TM = Ti, Zr, Hf) solid solutions is conducted in this work. It is shown that Ti atoms in a Mo solid solution are strong traps for oxygen atoms, while Hf and, even more clearly, Zr atoms are not. It is pointed out that the ionic and covalent interactions are the primary influence on the trapping behavior, as the change in ionic and covalent interactions between trapping and nontrapping models follows the trend Mo-1Ti > Mo-1Hf > Mo-1Zr, which resembles the trend of the trapping energy.

Keywords: Mo-based alloys; oxygen trapping; chemical bonding; density functional theory

1. Introduction

Structural materials based on refractory metals like molybdenum provide a high potential for a variety of ultra-high-temperature applications due to their outstanding strength and creep resistance; additionally, specific alloys form a self-protection surface layer during exposure to air [1–3].

Nevertheless, the room-temperature strength and ductility of pure and alloyed Mo is restricted by low grain-boundary cohesion [4–7]. This leads to higher ductile-to-brittle transition temperatures and an intergranular fracture mode [8–10], which limits the manufacturability and application of Mo-based alloys as structural materials.

It was found in multiple studies [8,11–14] that oxygen has a most significant impact on the embrittlement of pure Mo as well as in the presence of alloying elements. In [8], it was shown that the work of fracture is the function of the O segregation level at the grain boundary. Furthermore, it is worth mentioning that embrittlement at room temperature occurs at a relatively low O content, lying at around several dozens of ppm [8,15]. Auger electron spectroscopy [8] and atom probe tomography [16] reveal that oxygen segregates significantly on the grain boundary. The leading cause for that is believed to be low solubility [17], which lies at around 3.4 ppm at 1673 K [18]. The grain-boundary segregation also occurs in a state-of-the-art, technically pure Mo, as shown using atom probe tomography in [16].

Technically relevant Mo alloys are mainly designed as multiphase materials, e.g., composed of silicide or boride phases besides a Mo solid-solution phase. In such systems, the Mo solid-solution phase has a decisive role in achieving acceptable ductility. So,

to improve the ductility of Mo-based alloys, the following steps are recommended in the literature:

- Usage of high-purity raw materials [16].
- Preliminary heat treatment in a hydrogen atmosphere at higher temperatures and high pressure, which could be combined with a sintering step [19] or with high duration in near-vacuum conditions at high temperatures [8,20].
- Alloying with substitutional or interstitial elements [7,8,21].

Though the use of high-purity raw materials and heat treatment can provide the means to reduce the effect of the O-induced embrittlement, the O content can nevertheless increase significantly during the processing, for example, during welding [11–14], high-temperature forming [16], or additive manufacturing [9]. In Figure 1, the oxygen concentrations in various types of Mo-based alloys are presented, which were processed by different production routes, namely, ingot metallurgy, powder metallurgy, and additive manufacturing. It is obvious that the powder metallurgy, as well as additive manufacturing, typically results in high contamination and, therefore, high ductile-to-brittle transition temperatures. Typical sources for oxygen or processing steps when oxygen pick-up takes place, are, for example, the mechanical alloying process (used for prealloying powder mixtures by high-energy ball milling before sintering), a nonoptimized gas atomization process for the production of alloyed powders, the handling or storage of powders in oxygen-containing atmosphere, or residual oxygen in the process chamber for powder additive manufacturing. Optimizing these processes may help to reduce the overall oxygen concentration in bulk materials. Additionally, an interesting option is to directionally solidify Mo-based multiphase alloys in an inert atmosphere, which has the potential to produce bulk material with comparatively low oxygen concentrations (e.g., 32, . . . , 50 ppm) in a Mo-Si-B alloy [22]. However, it is well accepted that oxygen contamination cannot be entirely avoided during the technical processing of multiphase Mo alloys.
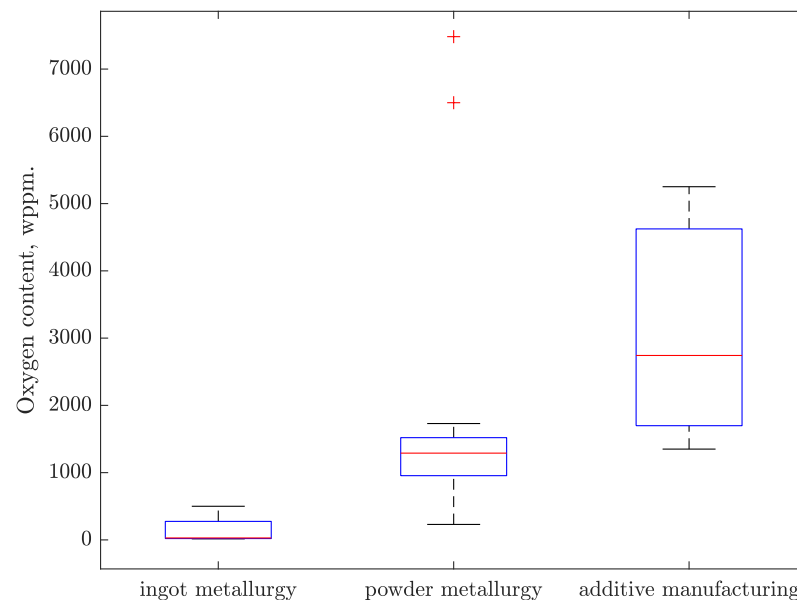

Figure 1. The oxygen content in Mo-based alloys as a result of different production routes. Sources for ingot metallurgy [23–29], powder metallurgy [9,21,25,28–32], and additive manufacturing [9,28].

In addition, Mo has a high affinity for oxygen at elevated temperatures [33], so during the high-temperature operation, an increase in the O in the Mo phase is inevitable. Thus, alloying strategies are the most plausible way to reduce the O-driven embrittlement in Mo-based alloys.

The group of such beneficial elements includes Ti, Zr, and Hf, which are attractive candidates for the design of single-phase and multiphase Mo-based alloys, for example,

in Mo-Ti-Si, Mo-Hf-B, Mo-Zr-B, and Mo-Si-B-Zr systems. The latter alloy systems have been shown to possess higher toughness as compared to other Mo-based alloys and, at the same time, a high creep resistance at temperatures higher than 1000 °C [34–37]. All of these alloys are multiphase. Nevertheless, the Mo-based solid solution is present as a microstructural constituent in considerable fraction, see Figure 2 (here, Mo solid-solution phases appear light gray in the micrographs due to the SEM/BSE contrast). It leads again to the question of grain/phase boundary cohesion. Therefore, the chemical composition of the solid-solution phase is the key factor in defining the ductility and toughness of multiphase technical Mo alloys. For this reason, the bonding situation and interaction of Mo atoms with the atoms of the alloying partners, as well as atoms of oxygen, will be investigated in detail in this work to draw important conclusions for the alloying design of high-potential prospective Mo alloys. Recently, several ab initio studies were conducted regarding the problem of low grain-boundary cohesion and oxygen segregation in Mo-based alloys. Scheiber et al. [38] investigated possible candidates for ductilization of Mo using a high-throughput density functional theory investigation. It was found that Zr, Ti, and Hf should increase grain-boundary cohesion, thus promoting ductile failure at lower temperatures. In contrast, in a later study [39], it was concluded that Hf should have a negative impact on grain-boundary cohesion, and interstitial elements like boron or carbon have the most positive impact on that. Oxygen, in contrast, was found to have a drastic negative impact on grain-boundary cohesion, which was expected based on the experimental data. In the study above, the first attempts at modeling simultaneous segregation were made as well. In [40], the segregation energies of light interstitial elements were estimated. It was concluded that interstitials tend to segregate at grain boundaries due to the low electron density. Furthermore, Reynolds et al. [41] studied a similar Nb-(X)-O system using the ab initio method. It was found that the Bader charge and lattice distortion are two main factors governing trapping energies in Nb–solid-solution bulk. The attractive interactions are favored by the elements with a positive Bader charge, resulting in the higher solubility of O in Nb-(TM) solid solutions as well as a lower O diffusion rate. This way, the O content on grain boundaries should be significantly reduced. Finally, Kumar et al. reported about the Si-O interaction in a Mo-Si solid solution with dissolved oxygen atoms using density functional theory (DFT) calculations [42]. They found out that the serrated flow is only present at elevated temperatures and showed that this is due to the oxygen-trapping silicon atoms in the Mo-Si solid solution, which affect the dynamic strain aging. A similar approach and an in-depth analysis of the chemical bonding situation in selected Mo-TM(-O) (TM = Ti, Zr, Hf) solid solutions will be conducted in this work.

(a)　　　　　　　　(b)　　　　　　　　(c)
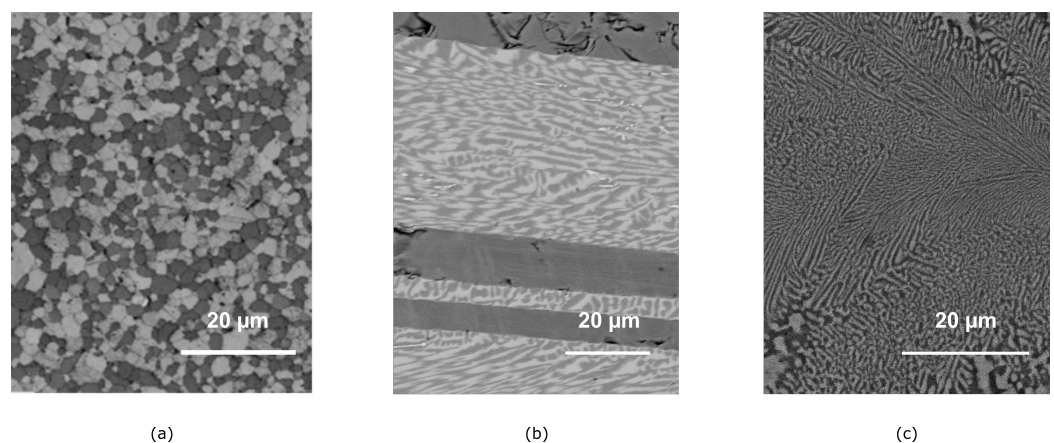
Figure 2. Multiphase microstructures of (**a**) Mo-Si-B-Ti alloy produced by powder metallurgical route, (**b**) directional solidified Mo-Hf-B, and (**c**) arc-casted eutectic Mo-Zr-B obtained by scanning electron microscopy.

2. Materials and Methods

The first-principles DFT calculations were carried out with Quantum ESPRESSO [43,44] for the structural relaxation of solid Mo and the Mo-xTM-yO (TM = Ti, Zr, Hf, x, y = 0, 1) solid solutions as 128- or 129-atom 4 × 4 × 4 supercells of Mo using PAW pseudopotentials [45] from the PSLibrary, version 1.0.0 [46]. The kinetic energy cut-off of the plane waves was set to 100 Ry, while the charge density and potential cut-off was set to 400 Ry. The structural relaxation stopped until a total energy convergence of 10^{-5} Ry and a force convergence of 10^{-4} Ry/a0 were reached. Marzari–Vanderbilt cold smearing [47] and a Gaussian spreading of 0.01 Ry were chosen to account for the Brillouin-zone integration in metals. The k-mesh was divided by 4 × 4 × 4 for the Mo-TM-O solid solutions using the Monkhorst–Pack algorithm [48]. Exchange and correlation in this DFT-based method were treated with the generalized gradient approximation (GGA) functional as parameterized by Perdew, Burke, and Ernzerhof (PBE-GGA) [49]. Quantum ESPRESSO was also used to generate the all-electron and valence-electron densities, which were then used to calculate the Bader charges and atomic volumina [50] according to the method described by Yu and Trinkle [51] with the CRITIC2 program [52,53].

The analysis of the chemical bonding was conducted on the most stable energy ground-state structures using the tight-binding, linear muffin-tin orbitals with the atomic spheres approximation (TB-LMTO-ASA) [54,55], as implemented in the TB-LMTO 4.7 program [56]. The Fermi level (EF) was set to 0 eV. The Monkhorst–Pack algorithm-generated k-mesh was 4 × 4 × 4 for the Mo-TM-O solid solutions. Exchange and correlation were treated with the PW91-GGA functional by Perdew et al. [57]. The bonding analysis was then carried out by calculation of the crystal orbital Hamilton population (COHP) [58] and its integrals (ICOHP). The ICOHP can be seen as a semiquantitative bonding energy that measures covalent contributions in solids.

In a 128-atom supercell with 1 substitutional TM atom (Mo-1TM), there are 6 trap sites (interstitial octahedral positions next to the substitutional TM atom) and 378 nontrapping interstitial sites. To calculate the temperature-dependent fraction of oxygen atoms trapped at the substitutional atom (Ti, Zr, or Hf), the trapping energy ΔE_{trap} was calculated first. The trapping energy can be defined as the energetic difference between the supercell with the O atom located at an interstitial octahedral position at the Ti, Zr, or Hf site, Mo-1TM-$1O_{\text{trapped}}$, and the supercell with the O atom at the position as far away as possible from the substitutional site, Mo-1TM-$1O_{\text{nontrapped}}$ (see also Figure 3). The resulting trapping energy ΔE_{trap} was then used in a Boltzmann-style formula [59] to gain the fraction of the oxygen atoms f_O at the trap site for a given temperature T:

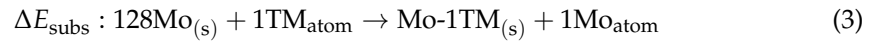$$f_O(T) = \frac{N_T N_{\text{NTS}} \exp\left(\frac{-\Delta E_{\text{trap}}}{K_B T}\right)}{N_{\text{NTS}} + N_T N_{\text{NTS}} \exp\left(\frac{-\Delta E_{\text{trap}}}{K_B T}\right)} \tag{1}$$

with N_T as the number of trapping atoms, N_{TS} as the number of trap sites, K_B as the Boltzmann constant, and N_{NTS} as the number of nontrap interstitial sites.
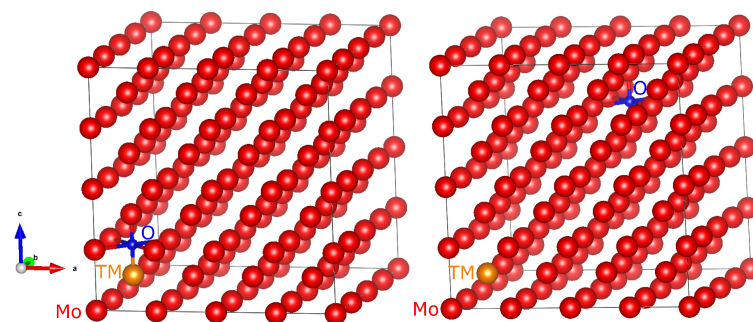
Figure 3. Used starting models of Mo-1TM-$1O_{\text{trapped}}$ (**left**) and Mo-1TM-$O_{\text{nontrapped}}$ (**right**) (TM = Ti, Zr, Hf), each before structural relaxation.

To calculate the formation enthalpies ΔH_f, substitutional ΔE_subst, and interstitial formation ΔE_inter energies at the ground state of Mo-1TM-1O (TM = Ti, Zr, Hf), the following three reactions were used:

$$\Delta H_\text{f} : 127\text{Mo}_{(s)} + 1\text{TM}_{(s)} + \frac{1}{2}\text{O}_{2_{(g)}} \rightarrow \text{Mo-1TM-1O}_{(s)} \tag{2}$$

$$\Delta E_\text{subs} : 128\text{Mo}_{(s)} + 1\text{TM}_\text{atom} \rightarrow \text{Mo-1TM}_{(s)} + 1\text{Mo}_\text{atom} \tag{3}$$

$$\Delta E_\text{inter} : \text{Mo-1TM}_{(s)} + 1\text{O}_\text{O} \rightarrow \text{Mo-1TM-1O}_{(s)} \tag{4}$$
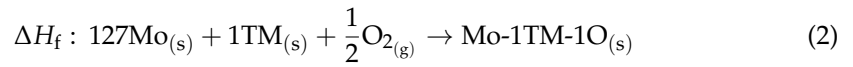
3. Results and Discussion

3.1. Temperature-Dependent Trapping of Oxygen Atoms

In this section, the trapping energy and the temperature-dependent trapping of oxygen atoms in Mo-1Ti, Mo-1Zr, and Mo-1Hf solid solutions will be discussed. In Table 1, the trapping energy is shown.

Table 1. Oxygen-trapping energy ΔE_trap of Mo-1Ti, Mo-1Zr and Mo-1Hf.

	Mo-1Ti	**Mo-1Zr**	**Mo-1Hf**
ΔE_trap (eV per cell)	−0.80	−0.15	−0.34

The oxygen-trapping energy is highest for Mo-1Ti and lowest for Mo-1Zr, putting the trapping energy of Mo-1Hf between the trapping energies of the two solid solutions mentioned above. Inserting the resulting oxygen-trapping energy in Equation (1) leads to the plots shown in Figure 4.
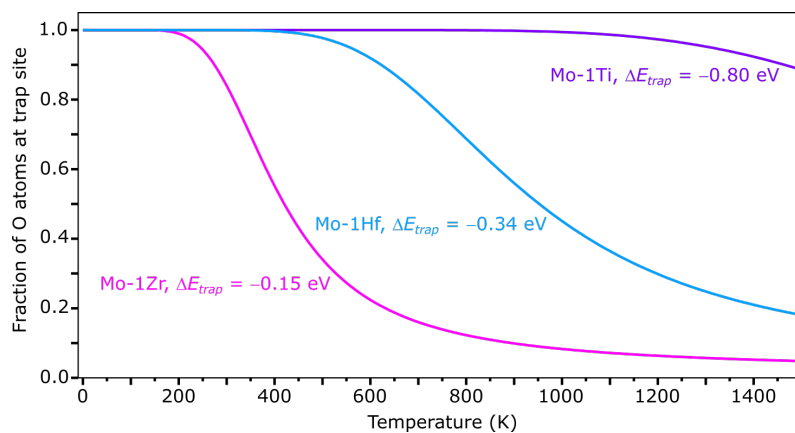
Figure 4. Temperature-dependent fraction of O atoms trapped at the substitutional atom Ti (purple), Zr (pink), or Hf (blue) in a Mo-1TM (TM = Ti, Zr, Hf) solid solution.

It is important to note that the following discussion holds only for concentrations of oxygen atoms lower than or equal to the concentration of substitutional atoms in these Mo-1TM solid solutions.

At 0 K, the probability of trapped oxygen atoms is 100% for all Mo-1TM solid solutions. At 300 K, this probability drops to 84% for Mo-1Zr and >99% for Mo-1Hf, while in Mo-1Ti, the probability remains at 100%. At 1500 K, the probability is 5% for Mo-1Zr, 18% for Mo-1Hf, and still 89% for Mo-1Ti.

Therefore, the probability of the occupation of trap sites by oxygen atoms decreases for the solid solutions Mo-1Zr, Mo-1Hf, and Mo-1Ti to 99% at different temperatures. For TM = Zr, this temperature is 200 K, while for TM = Hf it is 450 K and for TM = Ti it is 1060 K. For a probability of 90% of trapped oxygen atoms, the temperatures must be 270 K, 620 K, and 1460 K for Mo-1Zr, Mo-1Hf, and Mo-1Ti, respectively. In most cases, a probability of 10% nontrapped oxygen atoms (90% of O atoms at the trap site) should be

sufficient to feature a steady migration of oxygen atoms. Therefore, dynamic strain aging should start at low temperatures in Mo-1Zr, at slightly elevated temperatures in Mo-1Hf, and at clearly increased temperatures in Mo-1Ti. In the following sections, the reason for the different trapping behaviors will be discussed in terms of the respective formation enthalpies as well as the substitutional and interstitial energies. Furthermore, an analysis of the chemical bonding situation in the Mo-1TM-1O (TM = Ti, Zr, Hf) solid-solution models will be considered.

3.2. Formation Enthalpies and Substitutional and Interstitial Energies

In Table 2, the formation enthalpies (ΔH_f, Equation (2)), substitutional energies (ΔE_{subs}, Equation (3)), and interstitial formation energy (ΔE_{inter}, Equation (4)) of the solid solutions Mo-1TM-1O (TM = Ti, Zr, Hf) with the oxygen atom at the trap site are shown.

Table 2. Formation enthalpies and substitutional and interstitial formation energies at 0 K of Mo-1Ti-1O, Mo-1Zr-1O, and Mo-1Hf-1O.

	Mo-1Ti-1O	**Mo-1Zr-1O**	**Mo-1Hf-1O**
ΔH_f (kJ/mol per atom)	−1.19	−0.20	−0.57
ΔE_{subs} (eV per cell)	+0.14	−0.20	−0.79
ΔE_{inter} (eV per cell)	−3.92	−3.29	−3.48

The negative formation enthalpies ΔH_f of Mo-1Ti-1O, Mo-1Zr-1O, and Mo-1Hf-1O indicate that these compounds are stable. As the interstitial formation energy ΔE_{inter} is highly negative in all Mo-1TM-1O compounds, this gives a hint that the TM-O bond is very strong and might be the driving force of the formation of these solid solutions. Both ΔH_f and ΔE_{inter} of the Mo-1TM-1O solid solutions follow the trend already found with the trapping energy ΔE_{trap}. Interestingly, the substitutional energy ΔE_{subs} of Mo-1Ti is positive, suggesting that the bonding in Mo-1TM solid solutions between Mo and Ti is weaker than the Mo-Zr and Mo-Hf bonds.

3.3. Relaxed Crystal Structures and Bond Lengths

To investigate the different trapping behaviors in detail, one must first be sure that the chosen models are well suited to explain the chemical bonding situation. Therefore, the lattice parameters, the Mo-O and TM-O bond lengths, and the coordination numbers of Mo-1TM-1O with trapped and nontrapped oxygen atoms will be analyzed and compared with the situation in Mo-1O, a model with no TM atom in the lattice. Furthermore, it is necessary to take a closer look at the relaxed structures of the models Mo-1TM-1Otrapped and Mo-1TM-1Onontrapped (see Figure 5). In Table 3, the average lattice parameters, coordination numbers of oxygen, and Mo/Ti/Zr/Hf-O bond lengths are presented.

Table 3. Average lattice parameters a^*, coordination numbers (CNs), and Mo-O and TM-O atomic distances in Mo-1O and Mo-1TM-1O models with trapped and nontrapped oxygen atoms.

	Mo-1Ti-1O	**Mo-1Zr-1O**	**Mo-1Hf-1O**	**Mo-1O**
$a^*(O_T)$ [1] [Å]	3.1645	3.1679	3.1656	
$a^*(O_{NT})$ [2] [Å]	3.1652	3.1678	3.1674	3.1653
$CN(O_T)$	6	5 + 1	6	
$d(TM - O)$ [Å]	1.87	1.98	1.94	
$d(Mo - O_T)$ [Å]	1.96 − 2.26	1.92 − 2.29, 2.63	1.93 − 2.29	
$CN(O_{NT})$	5 + 1	5 + 1	5 + 1	5 + 1
$d(Mo - O_{NT})$ [Å]	1.94 − 2.25, 2.62	1.95 − 2.25, 2.61	1.95 − 2.25, 2.61	1.95 − 2.26, 2.63

[1] Here and further, T denotes a trapped state. [2] Here and further, NT denotes a nontrapped state.
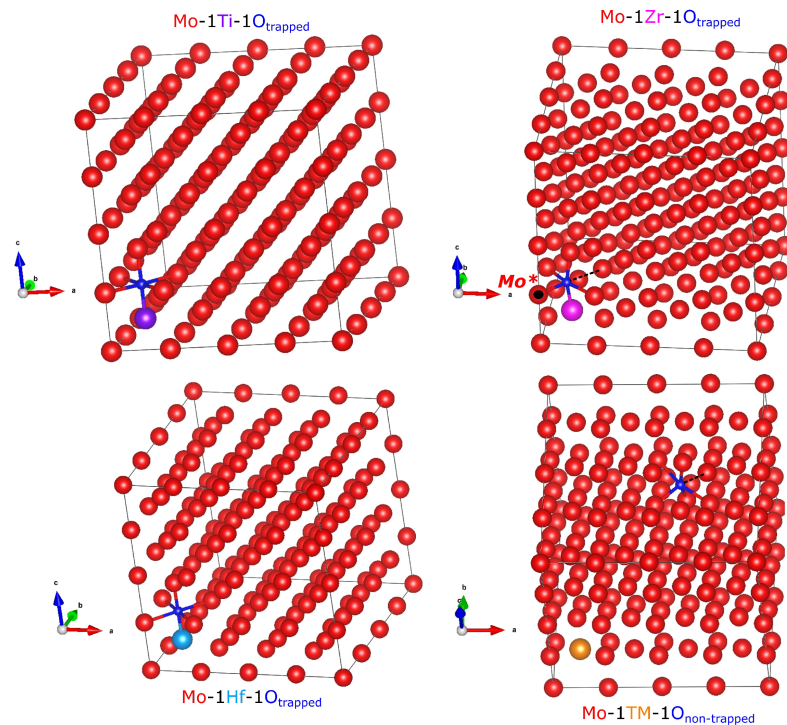
Figure 5. Structural relaxed models of Mo-1Ti-1O$_{trapped}$ (**top left**), Mo-1Zr-1O$_{trapped}$ (**top right**), Mo-1Hf-1O$_{trapped}$ (**bottom left**), and Mo-1TM-1O$_{nontrapped}$ (TM = Ti, Zr, Hf, **bottom right**) solid solutions. The black dot in the model of Mo-1Zr-1O$_{trapped}$ is used to mark the one Mo atom in equatorial position to the oxygen atom (also called Mo*) with an unusually short Mo-O distance. The dashed lines for the models Mo-1Zr-1O$_{trapped}$ and Mo-1TM-1O$_{nontrapped}$ show the long Mo-O bond in equatorial position to the oxygen atom.

For the lattice parameters in the nontrapping case, $a^*(O_{nontrapped})$, the trend is Mo-1Ti-1O $\approx$ Mo-1O $<$ Mo-1Hf-1O $\approx$ Mo-1Zr-1O, which resembles the trend of the atomic radii in crystals (Ti: 1.40 Å, Mo: 1.45 Å, Zr, Hf: 1.55 Å) reported in [60]. In the trapping case, the lattice parameter $a^*(O_{trapped})$ is unexpectedly smaller for Mo-1Ti-1O and Mo-1Hf-1O, while in the case of Mo-1Zr-1O, the difference is not significant as compared with the nontrapping case. This might give a hint that the overall bonding situation in the solid state systems Mo-1Ti-1O$_{trapped}$ and Mo-1Hf-O$_{trapped}$ could be stronger than in Mo-1Zr-1O$_{trapped}$. Taking a look at the coordination numbers and Mo-O bond lengths in the nontrapping case, there is hardly any difference between the Mo-1TM-1O$_{nontrapped}$ models and Mo-1O. This can be seen as a sign that the used Mo-1TM-1O$_{nontrapped}$ models are sufficient to describe the oxygen trapping in Mo-1TM solid solutions. In the trapping case, the coordination number of oxygen in Mo-1Zr-1O$_{trapped}$ (CN: 5 + 1) resulted from one particularly short (2.07 Å) and one especially long (2.63 Å) equatorial Mo-O bond length. In this case, the 5 + 1 coordination number indicates that there are five surrounding atoms with similar bond distances along with a much longer bond. Therefore, the Mo-O bond lengths differ from the Mo-O bonds in the other two trapping models Mo-1Ti-1O$_{trapped}$ and Mo-1Hf-1O$_{trapped}$ (CN: 6). Furthermore, regarding the TM-O bond for TM = Ti, Hf is remarkably shorter (1.87 Å and 1.94 Å, respectively) than expected, indicating strong interactions between Ti/Hf and O. This hypothesis of strong interactions, especially those of Ti/Hf and O, in Mo-1Ti-O$_{trapped}$ and Mo-1Hf-O$_{trapped}$, respectively, will be discussed in the next section.

3.4. Chemical Bonding Analysis

3.4.1. Ionic Bonding

In solid-state materials, a variety of chemical bonding types are present. In Mo-1TM-1O metallic bonding, ionic bonding and covalent bonding are expected, while the metallic

bonding should be similar in Mo-1Ti-1O, Mo-1Zr-1O, and Mo-1Hf-1O; as the majority of the atoms in the solid solution are Mo, the more localized ionic and covalent bonding should be different, especially with the bonds in the vicinity of the TM and O atoms. To check this hypothesis, the ionic bonding will be discussed first.

For the description of the ionic bonding, the atomic charges are needed. To define atomic charges, Bader's formalism "Atoms in Molecules" [50] comes in handy. In Table 4, the Bader charges of Mo, TM (TM = Ti, Zr, Hf), and O in different supercell models are shown.

Table 4. Bader charges of Mo, TM (TM = Ti, Zr, Hf), and O in Mo-1O, Mo-1TM, and Mo-1TM-1O.

	Bader Charge Mo (e) [1]	Bader Charge TM (e)	Bader Charge O (e)
Mo-1Ti-1O$_{trapped}$	-0.13 to $+0.21$	$+1.14$	-1.26
Mo-1Ti-1O$_{nontrapped}$	-0.10 to $+0.24$	$+1.06$	-1.23
Mo-1Ti	-0.10 to $<+0.05$	$+1.06$	
Mo-1Zr-1O$_{trapped}$	-0.14 to $+0.26$	$+1.20$	-1.25
Mo-1Zr-1O$_{nontrapped}$	-0.10 to $+0.24$	$+1.05$	-1.23
Mo-1Zr	-0.10 to $<+0.05$	$+1.06$	
Mo-1Hf-1O$_{trapped}$	-0.16 to $+0.24$	$+1.32$	-1.27
Mo-1Hf-1O$_{nontrapped}$	-0.16 to $+0.24$	$+1.32$	-1.27
Mo-1Hf	-0.12 to $<+0.05$	$+1.19$	
Mo-1O	<-0.10 to $+0.25$		-1.23

[1] Defines the range of Bader charge for Mo atoms.

The Bader charge of oxygen is clearly negative, while the Bader charge of the TM atoms is clearly positive in the Mo-1TM and Mo-1TM-1O compounds. This is expected, as the trend for the atomic Pearson electronegativity is TM (Ti : 3.45 eV, Zr : 3.64 eV, Hf : 3.8 eV) < Mo (3.9 eV) < O (7.54 eV) [61]. Most of the Mo atoms either carry a little positive charge if interacting with the oxygen atom ($+0.05$ e to $+0.26$ e) or are barely charged at all ($<\pm0.05$ e) if there is no oxygen atom in the first coordination shell. Surprisingly, in all Mo-1TM-1O$_{trapped}$ solid solutions, there are four of eight Mo atoms in the first coordination shell of TM and in trans-position to the oxygen atom with negative atomic charges (-0.13 e to -0.16 e) balancing locally the highly positive Bader charge of the TM atom. In Mo-1TM and Mo-1TM-1O$_{nontrapped}$, eight of eight Mo atoms in the first coordination shell of TM carry a negative Bader charge (-0.10 e to -0.12 e) to balance locally the positive charge of TM. Taking a closer look, the trapped oxygen atom carries a slightly more negative charge and the TM atoms a clearly more positive charge in Mo-1TM-1O$_{trapped}$ than in the nontrapped case Mo-1TM-1O$_{nontrapped}$. In fact, the Bader charges of oxygen and the TM atom are the same for Mo-1Ti-1O$_{nontrapped}$, Mo-1Zr-1O$_{nontrapped}$, and Mo-1Hf-1O$_{nontrapped}$ and can be compared with the Bader charge of oxygen in Mo-1O and the Bader charge of the TM atom in Mo-1TM. This is another sign that the chosen models are sufficient to describe trapped and nontrapped oxygen atoms in Mo-1TM compounds.

Unfortunately, the information about Bader charges cannot be used to calculate the strength of the ionic bonding within the cell directly as the atoms vibrate around their equilibrium position, and the amount of screening cannot be determined easily. One can, however, use the electron densities to estimate qualitatively the ionic bonding strength, as the electric potential energy is proportional to the difference in the charge density. To calculate the Bader electron density, one divides the number of electrons within the Bader atomic volumina with the Bader atomic volumina. The difference between the TM and O atomic electron density of the trapping and nontrapping models of Mo-1TM-1O can be seen in Table 5. The TM atoms of the trapping models of Mo-1Ti-1O, Mo-1Zr-1O, and Mo-1Hf-1O possess a higher Bader electron density than their nontrapping counterparts. In the nontrapping models of Mo-1TM-1O, the atomic electron density of oxygen is higher than in the trapping models. Indeed, the differences in the Bader electron density of both TM

and O atoms follow the trend Mo-1Ti-1O > Mo-1Hf-1O > Mo-1Zr-1O, resembling the observed trend for the trapping energy. Therefore, the ionic interactions might be higher in Mo-1Ti-1O than in Mo-1Hf-1O and Mo-1Zr-1O.

Table 5. Differences in the Bader atomic electron density (ρ) and the integrated crystal orbital Hamilton population (ICOHP) of the O-X bonds (X: Mo or TM) between oxygen-trapping and not-oxygen-trapping models of Mo-1Ti-1O, Mo-1Zr-1O, and Mo-1Hf-1O.

|	**Mo-1Ti-1O**	**Mo-1Zr-1O**	**Mo-1Hf-1O**
$\Delta\rho(\text{TM})$ (Å^{-3})	+0.061	+0.029	+0.035
$\Delta\rho(\text{O})$ (Å^{-3})	−0.031	−0.028	−0.029
$\Delta\text{ICOHP}(\text{O} - \text{X})$ (eV per cell)	−0.29	+0.36	−0.04

3.4.2. Covalent Bonding

As mentioned above, ionic bonding is only one type of the chemical bonds existing in the Mo-TM-O systems. If the integrated crystal orbital Hamilton populations (ICOHPs, semiquantitative covalent bonding energy) of the O-X bonds (X: Mo or TM) are also considered (see Table 5), the different trapping behaviors in terms of covalent bonding might be explained qualitatively in a similar manner as the ionic bonding described above. For the analysis of the ICOHPs, the O-TM (TM: Ti, Zr, Hf) and the O-Mo bonds in the trapping and nontrapping case are considered. The differences in the ICOHPs now show that the covalent bonding from the trapped to the nontrapped case becomes stronger for Mo-1Ti-1O, massively weaker for Mo-1Zr-1O, and a bit stronger for Mo-1Hf-1O. So again, the trend Mo-1Ti-1O > Mo-1Hf-1O > Mo-1Zr-1O is found for the covalent bonding strength situation, similar to the trend for the ionic interactions and the trapping energy. As a very good example of the covalent bonding situation in the trapping models, the TM-O bond in Mo-1TM-1O$_{\text{trapped}}$ is discussed. The ICOHP of the Ti-O bond is −2.63 eV. The Hf-O bond is stronger than the Ti-O bond (ICOHP: −2.92 eV), while the ICOHP of the Zr-O bond is considerably weaker than the Ti-O and Hf-O bonds with an ICOHP of −0.94 eV. Figure 6, left, shows the reason for this weak covalent bond.

In the Zr-O bond, antibonding states are occupied in the area from −7 eV to the Fermi level, destabilizing this bond heavily. In contrast, only a few occupied antibonding states for the Ti-O and Hf-O bonds are found mainly in the area from −1 eV to the Fermi level. This explains the relatively weak Zr-O but stronger Ti-O and Hf-O bonds, as antibonding states destabilize chemical bonding in general.

As the different oxygen-trapping behavior of the series Mo-1TM (TM = Ti, Zr, Hf) could be explained in terms of chemical bonding, the COHP technique might also explain the different coordination number of the oxygen atom in Mo-1Zr-1O$_{\text{trapped}}$. The assumption is that the 5 + 1 coordination of the oxygen atom in Mo-1Zr-1O$_{\text{trapped}}$ might be due to electronic reasons. The COHP plots shown in Figure 6, right, depict two cases of oxygen coordination in Mo-1Zr-1O. Assuming a coordination number of six for the oxygen atom, the model Mo-1Zr-1O-CN6 is created. For this model, the relaxed crystal structure of Mo-1Hf-1O$_{\text{trapped}}$ is used, in which Hf is replaced with Zr but no new structural relaxation is conducted. In the model Mo-1Zr-1O-CN6, the Mo atom, which was the former Mo* atom shown in Figure 5, top right, is now Mo**. The newly formed Mo**-O bond length is similar to the other equatorial Mo atoms in direct coordination with the oxygen atom at the trap site. Now taking a look at the chemical bonding situation of this Mo**-O bond (gray plot in Figure 6, right), there are antibonding states occupied from −2 eV to the Fermi level. This bond is not very stable because of the occupied antibonding states at the Fermi level. To remove this unstable bonding situation, the distance between the oxygen atom and the Mo** atom must change. In the case of the Mo** atom, the Mo-O bond length decreases from 2.29 Å to 2.07 Å, leading to increased interaction between these two atoms and a new type of bond (Mo*-O), and hence, the already known model Mo-1Zr-1O$_{\text{trapped}}$ is created (see Figure 5, top right). As a result, the COHP (black plot in Figure 6) now shows

areas of more bonding interactions, especially from $-5\,\mathrm{eV}$ to $-3\,\mathrm{eV}$. However, there is also an area of more antibonding states from $-2\,\mathrm{eV}$ to close to the Fermi level. The decisive change is now at the Fermi level, which reveals slight bonding states and, therefore, a more stable bonding situation of the Mo-O bond, in contrast to the aforementioned situation in Mo-1Zr-1O-CN6 with antibonding states at the Fermi level in this type of Mo-O bond. The shorter Mo*-O bond is not only more stable than the longer Mo**-O bond but also clearly stronger ($-2.69\,\mathrm{eV}$ vs. $-1.57\,\mathrm{eV}$). Therefore, the $5+1$ coordination of oxygen in Mo-1Zr-1O$_{\mathrm{trapped}}$ originates most likely from a stabilizing Mo-O bond in this compound.
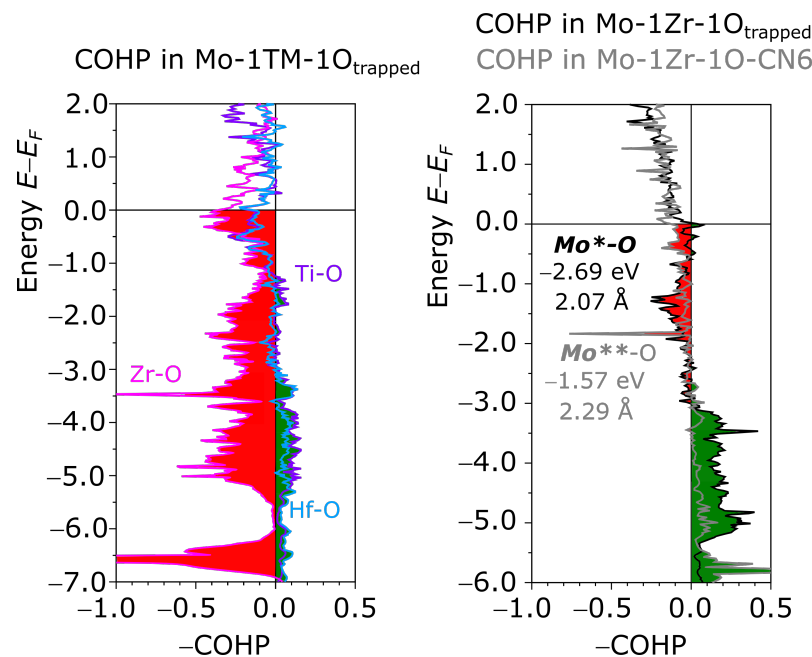
Figure 6. Left: COHP plots of the Ti-O bond (purple), the Zr-O bond (pink), and the Hf-O bond (blue) in Mo-1TM-1O$_{\mathrm{trapped}}$ (TM = Ti, Zr, Hf) models. **Right**: COHP plots of the Mo*-O bond (in black, short equatorial Mo-O bond in the model Mo-1Zr-1O$_{\mathrm{trapped}}$) and of the Mo**-O bond (in gray, usual equatorial Mo-O bond in the model Mo-1Zr-1O-CN6). Bonding states are filled green, while antibonding states are filled red.

4. Conclusions

The behavior of the Mo solid-solution phase plays a major role in controlling the ductility of multiphase Mo alloys. Specifically, oxygen contamination has a significant impact on the embrittlement of technically relevant alloys. Therefore, the oxygen-trapping behavior of Mo solid solutions, i.e., Mo-1Ti, Mo-1Zr, and Mo-1Hf, was investigated using DFT. With 129-atom supercells, it was shown that the oxygen-trapping energy follows the trend Mo-1Ti-1O > Mo-1Hf-1O > Mo-1Zr-1O, which means that even at high temperatures, oxygen atoms are trapped by Ti atoms and the dynamic strain aging effect is low. In contrast, low temperatures are sufficient to remove oxygen from Zr trap sites, promoting dynamic strain aging. The reason for this trapping behavior could be found within different mechanisms of the chemical bonding in the trapping and nontrapping models of Mo-1TM-1O. To summarize the chemical bonding situation in Mo-1TM-1O solid solutions, the difference in the ionic and covalent bonding strengths between the trapping and nontrapping models for the case of Mo-1Ti-1O might be the main driving force for the superior oxygen-trapping behavior. In contrast, the disastrous change in the covalent bonding strength between the trapping and nontrapping models of Mo-1Zr-1O explains this compound's rather inferior oxygen-trapping behavior. However, considerable ionic bonding is expected as well. For TM = Hf, the enhancement in ionic bonding and the somewhat slight improvement of the covalent bonding situation for the bonds containing oxygen in the trapping model compared with the nontrapping model puts the oxygen-

trapping behavior of Mo-1Hf right between those of Mo-1Ti and Mo-1Zr. The quantitative differences might appear after taking into account the exact ionic interactions between Mo, TM, and O. Although the exact strength of the ionic bonding could not be calculated, it was shown that the interplay of both the ionic and covalent bonding is responsible for the observed oxygen-trapping behavior of Mo-1TM solid solutions. Furthermore, it was explained that an unstable Mo-O bond is the driving force behind the formation of a 5 + 1 coordination of oxygen at the trap site in Mo-1Zr. The presented simulation results indicate the experimental trend observed in different previous experimental investigations. It was found that of the three investigated elements, Ti additions can ductilize molybdenum-based alloys [21], especially in combination with carbon. Furthermore, Zr and Hf were found to also contribute to ductilization, but these elements do not have such a significant impact on the investigated molybdenum-based materials at room temperature [7,24]. Though other factors should play a role in this case, especially solid-solution strengthening, titanium seems to be the most promising alloy candidate to increase the grain-boundary cohesion and reduce O content at the grain boundary [41] from all three investigated elements.

Nevertheless, the influence of TM elements on the solubility of oxygen in a Mo-based solid solution is unclear and needs to be investigated more thoroughly, as it is the main factor controlling the segregation level [17]. Furthermore, it was shown using TEM that the formation of TM oxide [7,21] and carbide [8] nanoparticles can induce dislocation generation at the grain boundary in Mo-based materials. Furthermore, it was shown that the aforementioned particles could increase the cohesion of grain boundaries [21]. It was assumed that the high matrix–particle coherence could play a role in forming more resilient bonds. Therefore, this issue should also be considered in further investigations.

Author Contributions: Conceptualization, R.S.T. and M.K.; methodology, R.S.T.; software, R.S.T.; validation, R.S.T., R.N. and M.K.; formal analysis, R.S.T. and R.N.; investigation, R.S.T.; resources, M.K.; data curation, R.S.T.; writing—original draft preparation, R.S.T., R.N. and M.K.; writing—review and editing, R.N. and M.K.; visualization, R.S.T. and R.N.; supervision, M.K.; project administration, R.S.T. and M.K.; funding acquisition, M.K. All authors have read and agreed to the published version of the manuscript.

Informed Consent Statement: Not applicable.

Data Availability Statement: The data presented in this study are available onrequest from the corresponding author (privacy).

Conflicts of Interest: The authors declare no conflicts of interest.

References

1. Soboyejo, W.; Srivatsan, T. *Advanced Structural Materials: Properties, Design Optimization, and Applications*; CRC Press: Boca Raton, FL, USA, 2006.
2. Schliephake, D.; Kauffmann, A.; Cong, X.; Gombola, C.; Azim, M.; Gorr, B.; Christ, H.J.; Heilmaier, M. Constitution, oxidation and creep of eutectic and eutectoid Mo-Si-Ti alloys. *Intermetallics* **2019**, *104*, 133–142. [CrossRef]
3. Perepezko, J.; Krüger, M.; Heilmaier, M. Mo-Silicide Alloys for High-Temperature Structural Applications. *Mater. Perform. Charact.* **2021**, *10*, 122–145. [CrossRef]
4. Brosse, J.; Fillit, R.; Biscondi, M. Intrinsic Intergranular Brittleness of Molybdenum. *Scr. Metall.* **1981**, *15*, 619–623. [CrossRef]
5. Tsurekawa, S.; Tanaka, T.; Yoshinaga, H. Grain Boundary Structure, Energy and Strength in Molybdenum. *Mater. Sci. Eng. A* **1994**, *176*, 341–348. [CrossRef]
6. Geller, C.B.; Smith, R.W.; Hack, J.E.; Saxe, P.; Wimmer, E. A computational search for ductilizing additives to Mo. *Scr. Mater.* **2005**, *52*, 205–210. [CrossRef]
7. Saage, H.; Krüger, M.; Sturm, D.; Heilmaier, M.; Schneibel, J.; George, E.; Heatherly, L.; Somsen, C.; Eggeler, G.; Yang, Y. Ductilization of Mo–Si solid solutions manufactured by powder metallurgy. *Acta Mater.* **2009**, *57*, 3895–3901. [CrossRef]
8. Kumar, A.; Eyre, B.L. Grain Boundary Segregation and Intergranular Fracture in Molybdenum. *Proc. R. Soc. A Math. Phys. Eng. Sci.* **1980**, *370*, 431–458. [CrossRef]

9.　Fichtner, D.; Schmelzer, J.; Yang, W.; Heinze, C.; Krüger, M. Additive Manufacturing of a Near-Eutectic Mo–Si–B Alloy: Processing and Resulting Properties. *Intermetallics* **2021**, *128*, 107025. [CrossRef]

10.　Schneibel, J.H.; Brady, M.; Kruzic, J.; Ritchie, R.O. On the Improvement of the Ductility of Molybdenum by Spinel (MgAl2O4) Particles. *Int. J. Mater. Res.* **2022**, *96*, 632–637. [CrossRef]

11.　Cockeram, B.V.; Ohriner, E.K.; Byun, T.S.; Miller, M.K.; Snead, L.L. Weldable Ductile Molybdenum Alloy Development. *J. Nucl. Mater.* **2008**, *382*, 229–241. [CrossRef]

12.　Zhang, Y.; Wang, T.; Jiang, S.; Zhang, B.; Wang, Y.; Feng, J. Microstructure Evolution and Embrittlement of Electron Beam Welded TZM Alloy Joint. *Mater. Sci. Eng. A* **2017**, *700*, 512–518. [CrossRef]

13.　Wang, T.; Zhang, Y.; Jiang, S.; Li, X.; Zhang, B.; Feng, J. Stress Relief and Purification Mechanisms for Grain Boundaries of Electron Beam Welded TZM Alloy Joint with Zirconium Addition. *J. Mater. Process. Technol.* **2018**, *251*, 168–174. [CrossRef]

14.　Wang, T.; Li, N.; Zhang, Y.; Jiang, S.; Zhang, B.; Wang, Y.; Feng, J. Influence of Welding Speed on Microstructures and Mechanical Properties of Vacuum Electron Beam Welded TZM Alloy Joints. *Vacuum* **2018**, *149*, 29–35. [CrossRef]

15.　Morito, F. Effect of Impurities on the Weldability of Powder Metallurgy, Electron-Beam Melted and Arc-Melted Molybdenum and Its Alloys. *J. Mater. Sci.* **1989**, *24*, 3403–3410. [CrossRef]

16.　Babinsky, K.; Weidow, J.; Knabl, W.; Lorich, A.; Leitner, H.; Primig, S. Atom Probe Study of Grain Boundary Segregation in Technically Pure Molybdenum. *Mater. Charact.* **2014**, *87*, 95–103. [CrossRef]

17.　Seah, M.P.; Hondros, E.D. Grain Boundary Segregation. *Proc. R. Soc. London. Ser. A Math. Phys. Sci.* **1973**, *335*, 191–212. . [CrossRef]

18.　Srivastava, S.C.; Seigle, L.L. Solubility and Thermodynamic Properties of Oxygen in Solid Molybdenum. *Metall. Trans.* **1974**, *5*, 49–52. [CrossRef]

19.　Azim, M.A.; Gorr, B.; Christ, H.J.; Heilmaier, M.; Koch, U.; Engelhard, M. Characterization of Oxidation Kinetics of Mo–Si–B–Based Materials. *Oxid. Met.* **2017**, *87*, 89–108. [CrossRef]

20.　Ono, K.; Moriyama, J. Deoxidation of High-Melting-Point Metals and Alloys in Vacuum. *Metall. Trans. B* **1982**, *13*, 241–249. [CrossRef]

21.　Kurishita, H.; Kitsunai, Y.; Hiraoka, Y.; Shibayama, T.; Kayano, H. Development of Molybdenum Alloy with High Toughness at Low Temperatures. *Mater. Trans. Jim* **1996**, *37*, 89–97. [CrossRef]

22.　Hasemann, G.; Bogomol, I.; Schliephake, D.; Loboda, P.; Krüger, M. Microstructure and creep properties of a near-eutectic directionally solidified multiphase Mo–Si–B alloy. *Intermetallics* **2014**, *48*, 28–33. [CrossRef]

23.　Stephens, J.R.; Witzke, W.R. Alloy softening in group via metals alloyed with rhenium. *J. Less Common Met.* **1971**, *23*, 325–342. [CrossRef]

24.　Stephens, J.R.; Witzke, W.R. Alloy Hardening and Softening in Binary Molybdenum Alloys as Related to Electron Concentration. *J. Less Common Met.* **1972**, *29*, 371–388. [CrossRef]

25.　Schneibel, J.H.; Liu, C.T.; Heatherly, L.; Kramer, M.J. Assessment of Processing Routes and Strength of a 3-Phase Molybdenum Boron Silicide (Mo5Si3-Mo5SiB2-Mo3Si). *Scr. Mater.* **1998**, *38*, 1169–1176. [CrossRef]

26.　Majumdar, S.; Kapoor, R.; Raveendra, S.; Sinha, H.; Samajdar, I.; Bhargava, P.; Chakravartty, J.K.; Sharma, I.G.; Suri, A.K. A Study of Hot Deformation Behavior and Microstructural Characterization of Mo–TZM Alloy. *J. Nucl. Mater.* **2009**, *385*, 545–551. [CrossRef]

27.　Obert, S.; Kauffmann, A.; Heilmaier, M. Characterisation of the Oxidation and Creep Behaviour of Novel Mo-Si-Ti Alloys. *Acta Mater.* **2020**, *184*, 132–142. [CrossRef]

28.　Zhou, W.; Tsunoda, K.; Nomura, N.; Yoshimi, K. Effect of Hot Isostatic Pressing on the Microstructure and Fracture Toughness of Laser Additive Manufactured Mosibtc Multiphase Alloy. *Mater. Des.* **2020**, *196*, 109132. [CrossRef]

29.　Hinrichs, F.; Kauffmann, A.; Schliephake, D.; Seils, S.; Obert, S.; Ratschbacher, K.; Allen, M.; Pundt, A.; Heilmaier, M. Flexible Powder Production for Additive Manufacturing of Refractory Metal-Based Alloys. *Metals* **2021**, *11*, 1723. [CrossRef]

30.　Jéhanno, P.; Heilmaier, M.; Kestler, H. Characterization of an Industrially Processed Mo-based Silicide Alloy. *Intermetallics* **2004**, *12*, 1005–1009. [CrossRef]

31.　Suzuki, M.; Nutt, S.R.; Aikin, R.M., Jr. Creep Behavior of an SiC-reinforced XDTM MoSi2 Composite. *Mater. Sci. Eng. A-Struct. Mater. Prop. Microstruct. Process.* **1993**, *162*, 73–82. [CrossRef]

32.　Schmelzer, J.; Rittinghaus, S.K.; Weisheit, A.; Stobik, M.; Paulus, J.; Gruber, K.; Wessel, E.; Heinze, C.; Krüger, M. Printability of Gas Atomized Mo-Si-B Powders by Laser Metal Deposition. *Int. J. Refract. Met. Hard Mater.* **2019**, *78*, 123–126. [CrossRef]

33.　Floquet, N.; Bertrand, O.; Heizmann, J.J. Structural and Morphological Studies of the Growth of MoO3 Scales during High-Temperature Oxidation of Molybdenum. *Oxid. Met.* **1992**, *37*, 253–280. [CrossRef]

34.　Bolbut, V.; Bogomol, I.; Bauer, C.; Krüger, M. Gerichtet erstarrte Mo-Zr-B-Legierungen/ Directionally solidified Mo-Zr-B alloys. *Mater. Werkst.* **2017**, *48*, 1113–1124. [CrossRef]

35.　Bolbut, V.; Bogomol, I.; Loboda, P.; Krüger, M. Microstructure and mechanical properties of a directionally solidified Mo-12Hf-24B alloy. *J. Alloys Compd.* **2018**, *735*, 2324–2330. [CrossRef]

36.　Krüger, M.; Schliephake, D.; Jain, P.; Kumar, K.; Schumacher, G.; Heilmaier, M. Effects of Zr additions on the microstructure and the mechanical behavior of PM Mo-Si-B alloys. *JOM* **2013**, *65*, 301–306. [CrossRef]

37.　Krüger, M.; Kauss, O.; Naumenko, K.; Burmeister, C.; Wessel, E.; Schmelzer, J. The potential of mechanical alloying to improve the strength and ductility of Mo–9Si–8B–1Zr alloys—Experiments and simulation. *Intermetallics* **2019**, *113*, 106558. [CrossRef]

38. Scheiber, D.; Pippan, R.; Puschnig, P.; Ruban, A.; Romaner, L. Ab-Initio Search for Cohesion-Enhancing Solute Elements at Grain Boundaries in Molybdenum and Tungsten. *Int. J. Refract. Met. Hard Mater.* **2016**, *60*, 75–81. [CrossRef]

39. Scheiber, D.; Romaner, L.; Pippan, R.; Puschnig, P. Impact of Solute-Solute Interactions on Grain Boundary Segregation and Cohesion in Molybdenum. *Phys. Rev. Mater.* **2018**, *2*, 093609. [CrossRef]

40. Ma, H.; Ding, X.; Zhang, L.; Sun, Y.; Liu, T.; Ren, Q.; Liao, Y. Segregation of Interstitial Light Elements at Grain Boundaries in Molybdenum. *Mater. Today Commun.* **2020**, *25*, 101388. [CrossRef]

41. Reynolds, C.; Pollock, T.M.; Van Der Ven, A. Solute-Solute Interactions in Dilute Nb-X-O Alloys from First Principles. *Acta Mater.* **2024**, *266*, 119621. [CrossRef]

42. Yu, X.; Li, Z.; Jain, P.; Gao, H.; Kumar, S. Effect of Si content on the uniaxial tensile behavior of Mo-Si solid solution alloys. *Acta Mater.* **2021**, *207*, 116654. [CrossRef]

43. Giannozzi, P.; Baroni, S.; Bonini, N.; Calandra, M.; Car, R.; Cavazzoni, C.; Ceresoli, D.; Chiarotti, G.L.; Cococcioni, M.; Dabo, I.; et al. QUANTUM ESPRESSO: A modular and open-source software project for quantum simulations of materials. *J. Physics Condens. Matter* **2009**, *21*, 395502. [CrossRef]

44. Giannozzi, P.; Andreussi, O.; Brumme, T.; Bunau, O.; Nardelli, M.B.; Calandra, M.; Car, R.; Cavazzoni, C.; Ceresoli, D.; Cococcioni, M.; et al. Advanced capabilities for materials modelling with Quantum ESPRESSO. *J. Physics Condens. Matter* **2017**, *29*, 465901. [CrossRef]

45. Blöchl, P.E. Projector augmented-wave method. *Phys. Rev. B* **1994**, *50*, 17953–17979. [CrossRef]

46. Dal Corso, A. Pseudopotentials periodic table: From H to Pu. *Comput. Mater. Sci.* **2014**, *95*, 337–350. [CrossRef]

47. Marzari, N.; Vanderbilt, D.; De Vita, A.; Payne, M.C. Thermal Contraction and Disordering of the Al(110) Surface. *Phys. Rev. Lett.* **1999**, *82*, 3296–3299. [CrossRef]

48. Monkhorst, H.J.; Pack, J.D. Special points for Brillouin-zone integrations. *Phys. Rev. B* **1976**, *13*, 5188–5192. [CrossRef]

49. Perdew, J.P.; Burke, K.; Ernzerhof, M. Generalized Gradient Approximation Made Simple. *Phys. Rev. Lett.* **1996**, *77*, 3865–3868. [CrossRef]

50. Bader, R.F.W. *Atoms in Molecules*; Oxford University Press: Oxford, UK, 1994.

51. Yu, M.; Trinkle, D.R. Accurate and efficient algorithm for Bader charge integration. *J. Chem. Phys.* **2011**, *134*, 064111. [CrossRef]

52. de-la-Roza, A.O.; Blanco, M.; Pendás, A.M.; Luaña, V. Critic: A new program for the topological analysis of solid-state electron densities. *Comput. Phys. Commun.* **2009**, *180*, 157–166. [CrossRef]

53. de-la-Roza, A.O.; Johnson, E.R.; Luaña, V. Critic2: A program for real-space analysis of quantum chemical interactions in solids. *Comput. Phys. Commun.* **2014**, *185*, 1007–1018. [CrossRef]

54. Andersen, O.; Skriver, H.; Nohl, H.; Johansson, B. Electronic structure of transition metal compounds; Ground-state properties of the 3d-monoxides in the atomic sphere approximation. *Pure Appl. Chem. VI* **1980**, *52*, 93–118. [CrossRef]

55. Andersen, O.K.; Jepsen, O. Explicit, First-Principles Tight-Binding Theory. *Phys. Rev. Lett.* **1984**, *53*, 2571–2574. [CrossRef]

56. Jepsen, O.; Andersen, O. TB-LMTO-ASA (version 47), 2000.

57. Perdew, J.P.; Chevary, J.A.; Vosko, S.H.; Jackson, K.A.; Pederson, M.R.; Singh, D.J.; Fiolhais, C. Atoms, molecules, solids, and surfaces: Applications of the generalized gradient approximation for exchange and correlation. *Phys. Rev. B* **1992**, *46*, 6671–6687. [CrossRef]

58. Dronskowski, R.; Blöchl, P. Crystal orbital Hamilton populations (COHP): Energy-resolved visualization of chemical bonding in solids based on density-functional calculations. *J. Phys. Chem.* **1993**, *97*, 8617–8624. [CrossRef]

59. Maroef, I.; Olson, D.L.; Eberhart, M.; Edwards, G.R. Hydrogen trapping in ferritic steel weld metal. *Int. Mater. Rev.* **2002**, *47*, 191–223. [CrossRef]

60. Slater, J.C. Atomic Radii in Crystals. *J. Chem. Phys.* **2004**, *41*, 3199–3204. [CrossRef]

61. Pearson, R. Absolute Electronegativity and Hardness: Application to Inorganic Chemistry. *Inorg. Chem.* **1988**, *27*, 734–740. [CrossRef]